Deep Learning Based Automated Wound Detection for Clinical Image Analysis

[1]Ketan Kanjiya, [2]Piyush Sonani, [3]Upendrasinh Zala

[1]Chief Research Officer, [2]Chief Technology Officer, [3]Chief Executive Officer
[1]Information Technology Department,
[1]Kshatrainfotech Pvt Ltd, Ahmedabad, India
[1]ketan@neuramonks.com, [2]piyush@neuramonks.com, [3]upen@neuramonks.com

***Abstract*—Accurate and objective wound assessment is essential for effective clinical management, yet manual evaluation remains subjective, time consuming, and dependent on clinician expertise. In this study, we investigate a deep learning–based approach for automated wound segmentation and measurement using RGB images. A dataset of 3,960 wound photographs, combining three publicly available sources with clinically acquired images, was uniformly annotated at the pixel level and used to train an Attention U-Net model for robust wound boundary delineation. To enable real world dimensional analysis, a calibration marker placed adjacent to the wound is detected and utilized to estimate pixel to centimeter scale following geometric normalization. The segmented wound region is subsequently analyzed to compute key quantitative metrics, including area, perimeter, width, and height. Experimental evaluation demonstrates that the proposed approach provides accurate and consistent wound measurements across diverse clinical imaging conditions. These results highlight the potential of learning based segmentation combined with image based geometric analysis to support more objective wound assessment in clinical practice.**

***Index Terms*—Wound Detection, U-Net, Medical Imaging, Deep Learning, Segmentation, Pixel size calibration**

I. INTRODUCTION

Chronic wounds represent a substantial and growing burden on global healthcare systems, contributing to prolonged physical discomfort, psychological distress, and considerable long-term treatment costs [1]. Multiple studies estimate that close to one billion individuals worldwide are affected by both acute and chronic wounds [2,3]. In contrast to acute wounds, chronic wounds often exhibit slow and unpredictable healing trajectories, requiring continuous monitoring to prevent severe complications such as infection, hospitalization, and limb amputation [4].

Accurate and reliable wound assessment is therefore essential for guiding appropriate clinical interventions and monitoring healing progression. However, traditional wound assessment methods primarily visual inspection, manual ruler based measurements, and clinician dependent subjective evaluation remain susceptible to inconsistencies, inter-observer variability, and measurement inaccuracies [5,6]. Such subjectivity presents a major barrier to achieving standardized, reproducible, and high quality wound care.

To address these limitations, recent advances in Artificial Intelligence (AI) and Deep Learning (DL) have provided promising solutions for automating and standardizing wound assessment procedures [7-9]. The foundational step in any automated wound analysis system is wound segmentation, which involves accurately delineating wound regions from surrounding skin and background tissue. This step is critical because all downstream quantitative measurements including area, perimeter, and shape based metrics depend directly on segmentation quality [10]. Convolutional Neural Networks (CNNs) have demonstrated strong performance in this domain [11, 12], effectively capturing diverse wound textures, irregular boundaries, and imaging variations present in real clinical settings [13-15].

However, segmentation alone is insufficient for obtaining clinically meaningful measurements. While CNN based approaches can extract features such as wound length, width, and area in pixel units, converting these measurements into real world dimensions (cm^2 and cm) still requires a reference scale within the image. Without such calibration, automated measurements remain approximate and clinically unusable.

To overcome this limitation, the present study develops an integrated wound analysis framework that combines state-of-the-art deep learning based segmentation with a robust geometric calibration pipeline. By utilizing a green circular reference marker placed adjacent to the wound, our system performs automatic scale extraction, perspective normalization, and artifact removal, followed by precise wound segmentation using an Attention U-Net. This enables accurate computation of clinically relevant wound metrics including area, perimeter, width, and height in real world units directly from RGB images.

Overall, this work aims to deliver a computationally efficient and clinically applicable solution for automated wound assessment, offering substantial improvements over traditional manual procedures and enabling potential integration into remote care, telemedicine platforms, and future mobile wound monitoring systems [16, 17]. The remainder of this paper presents the dataset used, outlines the proposed methodology in detail, evaluates quantitative performance across multiple metrics, and discusses the broader implications of deploying such a system in practical clinical environments.

II. DATASET

(A) Dataset Collection

To develop a robust wound segmentation model, a diverse and representative dataset was constructed by integrating publicly available wound image sources with clinically acquired samples. A total of 2,760 images were collected from three publicly accessible datasets: the Medetec Wound Database [18], the Wound Image Dataset from Scientific Reports [19], and the Wound Segmentation Dataset [20]. These datasets collectively contain wound images captured under varying lighting conditions, camera types, and clinical environments. The images present substantial variability in wound color, size, boundary clarity, and surrounding skin texture, making them suitable for training a generalizable segmentation model.

(B) Image Preprocessing

To ensure uniformity across heterogeneous sources, all images were resized to a standardized resolution of 256 × 256 pixels while preserving essential wound details. Images were further normalized to reduce differences in illumination and color distribution across datasets.

(C) Annotation Procedure

To ensure consistent and high quality pixel-level labels across the entire dataset, all 3,960 wound images including the 2,760 publicly sourced images and the 1,200 clinically collected images were manually annotated under a unified framework. Annotation was performed using the Computer Vision Annotation Tool (CVAT) [21]. A few examples from the dataset are presented in figure 1. Each example includes the raw wound image and its corresponding pixel-level segmentation mask are shown directly below each image.

Figure 1: Examples of annotated wound images from the dataset, showing wound images (top row) and their corresponding pixel-level segmentation masks (bottom row)

III. Methodology

3.1) Deep Learning Model for Wound Segmentation

(A) Model Architecture

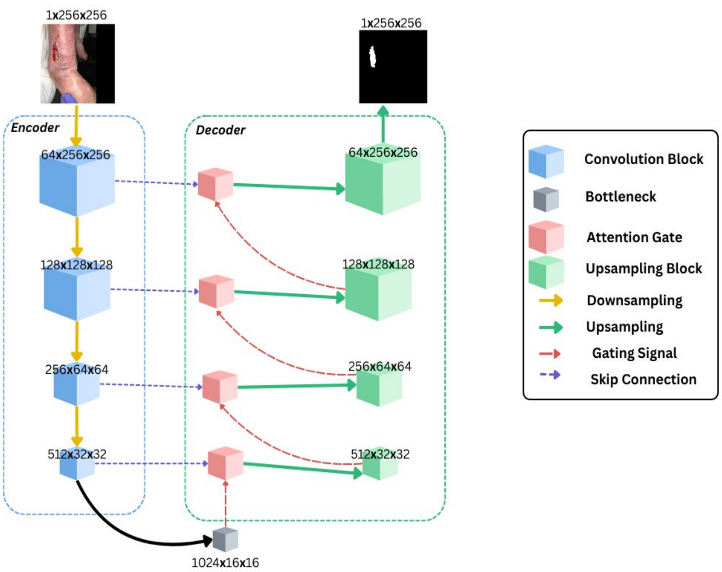

Figure 2: Architecture of the wound segmentation model

For wound segmentation, we employed an Attention U-Net [22], an extension of the standard U-Net architecture enhanced with attention gating mechanisms. The network consists of an encoder decoder structure with symmetric skip connections. Our Model is shown in figure 2.

The encoder is composed of five convolutional blocks, each containing two 3×3 convolutions followed by Batch Normalization and ReLU activation. Spatial downsampling is performed using 2×2 max-pooling. The decoder mirrors this structure, using upsampling operations followed by convolutional blocks to progressively reconstruct spatial resolution.

Attention Gates (AGs) are integrated into each skip connection to suppress irrelevant background features and emphasize salient wound regions. Each attention block computes a spatial attention coefficient using the gating signal from the decoder and feature maps from the encoder. The attended features are then concatenated with the decoder outputs, allowing the network to focus on clinically meaningful boundaries and tissue structures [23].

The final segmentation map is generated using a 1×1 convolution with a single output channel, suitable for binary wound and non-wound classification.

(B) Weight Initialization

All convolutional and linear layers were initialized using normal initialization with a gain of 0.02 to promote stable convergence. Batch normalization layers were initialized with unit variance. This initialization strategy ensures consistent weight scaling throughout the network and improves early stage training stability.

(C) Training Procedure

We used an NVIDIA GeForce RTX 4090 GPU to speed up parameter learning and evaluated the learned model on a computer with AMD Ryzen 7 5700X CPU. The program runs on a 64-bit Ubuntu operating system.

Training was performed using binary cross-entropy with logits, which combines a sigmoid layer with a binary cross-entropy objective. This loss function is well suited for medical segmentation tasks involving imbalanced wound–background pixel distributions.

The model was optimized using the Adam optimizer [24] with a learning rate of 1×10^{-3} and a batch size of 32. Training was executed for up to 1000 epochs, with early stopping based on validation loss to prevent overfitting. A patience value of 100 epochs was used, meaning training terminated when the validation loss failed to improve over 100 consecutive epochs.

During training, each batch consisted of paired (image, mask) samples. The forward pass generated segmentation logits, the loss was computed against the ground truth mask, and gradients were backpropagated to update model parameters.

3.2) Image-Based Wound Measurement and Analysis Pipeline

Our approach estimates wound area from RGB images using a two stage pipeline: geometric correction and scale estimation using a green calibration dot, followed by deep-learning based segmentation and contour based geometric analysis. The complete workflow is illustrated in figure 3.

3.2.1) Overview

Given an input wound image, we first detect a green calibration dot of known physical diameter placed adjacent to the wound. This marker provides:

a) A reference scale for converting pixel measurements to real world units, and
b) A geometric anchor for correcting perspective distortion.

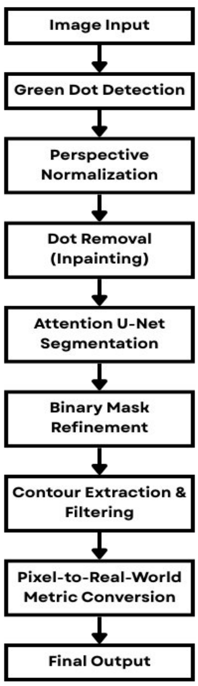

Figure 3: Workflow of the proposed wound analysis approach.

After estimating the scale and normalizing the image geometry, the calibration dot is removed via inpainting. An Attention U-Net is then applied to segment the wound region. Subsequent contour extraction and geometric computations yield the wound area, perimeter, width, and height in centimetres.

3.2.2) Green Dot Detection and Perspective Normalization

3.2.2.1) Green Dot Extraction (HSV Masking)

Each input image is converted to the HSV color space. A binary mask M(x,y) is generated by thresholding pixels whose hue falls within a predefined green range (Eq. 1), where H(x,y) is the pixel's hue value and Hmin, Hmax denote the chosen green range limits. Pixels satisfying the threshold are assigned M(x,y)=1 (green), and all others are set to M(x,y)=0. Contours are then extracted from this mask, and the largest green region is selected as the dot candidate.

$$M(x,y) = \begin{cases} 1, \, if \; H_{min} \leq H(x,y) \leq H_{max} \\ 0, \, otherwise \end{cases} \tag{1}$$

3.2.2.2) Circularity Verification

To ensure that the detected region corresponds to the circular marker, shape circularity is computed using Eq. (2), where A and P denote the contour area and perimeter, respectively. A perfect circle yields C=1, and regions with 0.7≤C≤0.9 are accepted as sufficiently circular.

$$C = \frac{4\pi A}{P^2} \tag{2}$$

The pixel area of the dot is:

$$A_{dot}^{px} = Area\left(C_{dot}\right) \tag{3}$$

3.2.2.3) Perspective Correction via Homography

If the detected dot deviates from circularity beyond a predefined threshold, a homography based top-view correction is applied. Let I be the input image, and H the estimated homography matrix:

$$I' = H(I) \tag{4}$$

This transformation ensures that both the calibration dot and the wound region exhibit correct geometric proportions. At this stage, we obtain the corrected image, the final dot contour, and the true area of the green reference marker.

3.2.3) Green Dot Removal via Inpainting

To prevent the segmentation network from misclassifying the calibration dot as wound tissue, the dot region is removed using mask guided inpainting.

3.2.4) Wound Segmentation Using Attention U-Net

The cleaned image is passed to a pretrained Attention U-Net for wound segmentation. The model outputs a grayscale mask M, which is thresholded to a binary mask:

$$M_{bin}(x,y) = \begin{cases} 1, \; if \; M(x,y) > 127 \\ 0, \; otherwise \end{cases} \tag{5}$$

To further refine this mask, morphological opening and closing are applied to remove residual noise and fill small gaps in the segmented wound region.

3.2.5) Contour Extraction and Filtering

Contours C_i are extracted from the processed mask. For each contour, the pixel area is computed.

$$A_i^{px} = Area(C_i) \tag{6}$$

To eliminate noise or small false positives, only contours that satisfy (Eq. 7) are retained. Here, A_{max}^{px} denotes the area of the largest contour, and α represents the contour threshold percentage.

$$A_i^{px} \geq \alpha \cdot A_{max}^{px} \tag{7}$$

3.2.6) Pixel-to-Real-World Area Conversion

The real world diameter of the green dot is a known constant Ddot (in cm). Its actual area is:

$$A_{dot}^{cm} = \pi \left(\frac{D_{dot}}{2} \right)^2 \tag{8}$$

The pixel to centimetre area conversion factor is:

$$R = \frac{A_{dot}^{cm}}{A_{dot}^{px}} \tag{9}$$

Thus, for the wound contour Cw with pixel area A_w^{px}, the real world wound area becomes:

$$A_w^{cm} = A_w^{px} \cdot R \tag{10}$$

3.2.6.1) Perimeter and Linear Measurements

Let P_w^{px} be the pixel perimeter of the wound contour. Real world perimeter is computed as:

$$P_w^{cm} = P_w^{px} \cdot \sqrt{R} \tag{11}$$

Similarly, bounding box width (Wpx) and height (Hpx) are converted as:

$$W_{cm} = W_{px} \cdot \sqrt{R} \tag{12}$$

$$H_{cm} = H_{px} \cdot \sqrt{R} \tag{13}$$

IV. Results

The performance of the proposed segmentation model was evaluated using two standard metrics: the Dice Similarity Coefficient (DSC) and the Intersection over Union (IoU).

Dice Similarity Coefficient (DSC):

Also known as the F1-score, the DSC is widely used in medical image analysis to quantify the degree of overlap between the predicted segmentation and the corresponding ground truth mask [25].

$$Dice = \frac{2\left|P \cap G\right|}{|P| + |G|} \tag{14}$$

Intersection over Union (IoU):

Also referred to as the Jaccard Index, IoU measures the similarity between the predicted and ground truth segmentation masks [26]. It is computed as the ratio of the area of intersection to the area of union of the two masks. Higher IoU values indicate better segmentation performance.

$$IoU = \frac{\left|P \cap G\right|}{\left|P \cup G\right|} \tag{15}$$

Here, P denotes the predicted binary segmentation mask generated by the model, and G denotes the ground truth binary mask provided by expert annotation. Both masks are represented as binary images, where P=1 and G=1 correspond to wound pixels, and P=0 and G=0 correspond to background pixels.

We additionally trained U-Net [27], ResUNet and R2U-Net [28] models to establish comparative baselines. As summarized in table 1, Attention U-Net achieved the best performance considering Dice based loss and IoU scores among all evaluated architectures, and was therefore selected as the final model for the proposed wound segmentation framework.

Table 1: Performance comparison of segmentation models

Model	Test Set Dice (%)	Test Set IoU (%)
U-Net	86.7	78.2
ResUNet	89.5	81.0
R2U-Net	88.9	80.3
Attention U-Net	**91.8**	**84.1**

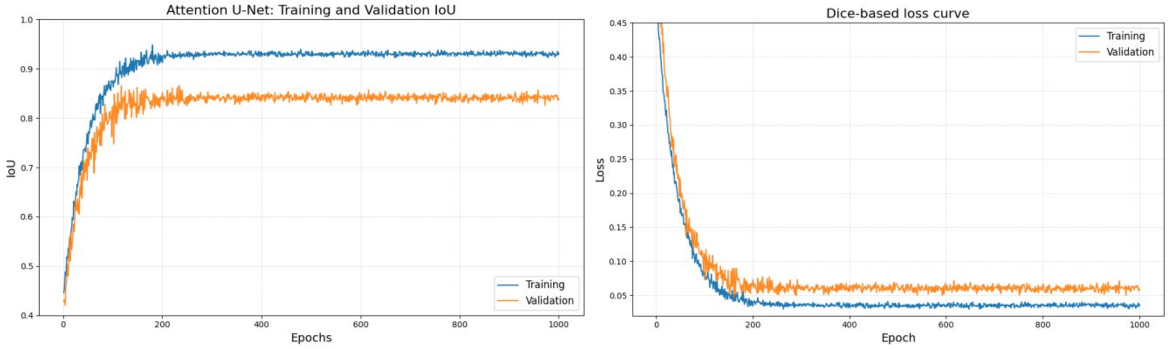

Figure 4: Training and validation curves, including Dice-based loss and IoU.

The training dynamics of the Attention U-Net are illustrated in figure 4. The IoU curve shows a rapid increase during the initial epochs, followed by gradual convergence as training progresses. Similarly, the Dice-based loss curve demonstrates a steep decline in the early training phase, with both training and validation losses decreasing consistently before stabilizing. The validation loss remains slightly higher than the training loss, which is expected due to dataset variability, yet the overall gap remains small, confirming stable optimization behavior.

Overall, the smooth convergence of IoU and loss curves suggests that the model effectively learns discriminative features for wound segmentation and maintains stable generalization across validation samples.

For quantitative validation, the wound areas estimated by the proposed method were compared against manually measured ground truth areas. Manual measurements were obtained through expert annotation, while computer estimated areas were computed using the calibrated pixel to centimeter conversion derived from the detected reference marker. The absolute percentage error between the two measurements was calculated using:

$$Error\,(\%) = \frac{|M - C|}{M} \times 100 \qquad (16)$$

where ,M denotes the manually measured wound area and C represents the computer estimated area.

Table 2 summarizes the results for all evaluated cases. As shown, the automated measurements closely match the manual measurements across the majority of samples, demonstrating the reliability and accuracy of the proposed wound area estimation approach.

Table 2. Comparison between manually measured wound areas and the areas estimated by the proposed method, along with the corresponding percentage error for 15 cases.

Case No.	Manually measured area (cm²)	Computer measured area (cm²)	Error (%)
1	32.84	33.12	0.85
2	5.12	4.82	5.86
3	0.52	0.5	3.85
4	68.47	55.92	18.33
5	14.96	15.08	0.8
6	2.41	2.34	2.9
7	301.22	301.4	0.06
8	8.12	7.65	5.78
9	7.04	6.87	2.41
10	58.94	54.29	7.89
11	11.42	10.98	3.85
12	16.25	16.1	0.92
13	70.38	68.32	2.93
14	1.31	1.29	1.53
15	17.02	17.45	2.53

To qualitatively demonstrate the performance of the proposed framework, figure 5 presents a comparison between the original wound image (containing the green calibration dot) and the final processed output. The output image shows the segmented wound region highlighted with a contour based boundary, along with the automatically computed wound area overlaid on the image. This visualization confirms that the model accurately localizes the wound and that the geometric calibration step enables reliable area estimation.

Figure 5: Comparison of the original wound image (above) and the final output generated by the proposed method (below), showing the delineated wound boundary and the computed wound area.

V. Conclusion

This study demonstrates that a deep learning based framework can reliably automate surface level wound assessment from standard RGB images. By integrating an Attention U-Net segmentation model with a green calibration marker, the proposed system achieves accurate and reproducible quantification of wound characteristics, including area, perimeter, width, and height. The combination of pixel level segmentation and geometric calibration enables robust measurement across diverse imaging conditions, as confirmed through both quantitative and qualitative evaluations. Importantly, the system is designed as a clinical decision support tool rather than a replacement for clinician expertise.

Future improvements could further enhance the system's clinical utility. These include incorporating multi-class tissue segmentation to provide more detailed wound characterization and adding temporal analysis modules to track healing over time. Moreover, validating the framework on larger, multi-center clinical datasets would help ensure stronger generalizability and real world reliability.

References

[1] R. Zhang, D. Tian, D. Xu, W. Qian, and Y. Yao, "A survey of wound image analysis using deep learning: classification, detection, and segmentation," IEEE Access, vol. 10, pp. 79502–79515, 2022.

[2] C. K. Sen, "Human wound and its burden: updated 2020 compendium of estimates," Adv. Wound Care, vol. 10, pp. 281–292, 2021.

[3] M. Edmonds, C. Manu, and P. Vas, "The current burden of diabetic foot disease," J. Clin. Orthop. Trauma, vol. 17, pp. 88–93, 2021.

[4] X. Liu, C. Wang, F. Li, X. Zhao, E. Zhu, and Y. Peng, "A framework of wound segmentation based on deep convolutional networks," in Proc. 10th Int. Congr. Image and Signal Processing, BioMedical Engineering and Informatics (CISP-BMEI), 2017.

[5] T. Biswas, M. F. M. A. Fauzi, F. S. Abas, and H. K. R. Nair, "Label card segmentation and calibration for computerized wound measurement system," in Proc. IEEE 8th R10 Humanitarian Technology Conf. (R10-HTC), 2020, pp. 1–6.

[6] S. Chairat, S. Chaichulee, T. Dissaneewate, P. Wangkulangkul, and L. Kongpanichakul, "AI-assisted assessment of wound tissue with automatic color and measurement calibration on images taken with a smartphone," Healthcare, vol. 11, p. 273, 2023.

[7] R. Niri, S. Zahia, A. Stefanelli, K. Sharma, S. Probst, S. Pichon, and G. Chanel, "Wound segmentation with U-Net using a dual attention mechanism and transfer learning," J. Imaging Informatics Med., vol. 38, pp. 3351–3365, 2025.

[8] Z. Liu, J. John, and E. Agu, "Diabetic foot ulcer ischemia and infection classification using EfficientNet deep learning models," IEEE Open J. Eng. Med. Biol., vol. 3, pp. 189–201, 2022.

[9] G. Scebba, L. Cicalò, D. Squarzoni, C. Caccianiga, A. Molinaro et al., "Detect-and-segment: a deep learning approach to produce wound segmentation," Informatics in Medicine Unlocked, 2022.

[10] H. Carrión, M. Jafari, M. D. Bagood, H.-Y. Yang, R. R. Isseroff, and M. Gomez, "Automatic wound detection and size estimation using deep learning algorithms," PLoS Comput. Biol., vol. 18, no. 3, p. e1009852, 2022.

[11] B. Cassidy, C. Kendrick, N. D. Reeves, J. M. Pappachan, and M. H. Yap, "Deep learning in chronic wound segmentation: a comprehensive review and meta-analysis," The Visual Computer, vol. 41, pp. 11885–11908, 2025.

[12] L. Maurya and S. Mirza, "MCTFWC: a multiscale CNN-transformer fusion based model for wound image classification," Signal, Image and Video Processing, vol. 19, p. 574, 2025.

[13] B. Song and A. Saçan, "Automated wound identification system based on image segmentation and artificial neural networks," in Proc. IEEE Int. Conf. Bioinformatics and Biomedicine (BIBM), 2012, pp. 1–4.

[14] D. Marijanović, E. K. Nyarko, and D. Filko, “Wound detection by simple feedforward neural network,” Electronics, vol. 11, no. 3, p. 329, 2022.

[15] D. M. Anisuzzaman, Y. Patel, B. Rostami, J. Niezgoda, S. Gopalakrishnan, and Z. Yu, “Multi-modal wound classification using wound image and location by deep neural network,” Scientific Reports, vol. 12, p. 20057, 2022.

[16] C. Wang, D. M. Anisuzzaman, V. Williamson, M. K. Dhar, B. Rostami, J. Niezgoda, S. Gopalakrishnan, and Z. Yu, “Fully automatic wound segmentation with deep convolutional neural networks,” Scientific Reports, vol. 10, p. 21897, 2020.

[17] A. Wagh, S. Jain, A. Mukherjee, E. Agu, P. C. Pedersen, D. Strong, B. Tulu, C. Lindsay, and Z. Liu, “Semantic segmentation of smartphone wound images: comparative analysis of AHRF and CNN-based approaches,” IEEE Access, vol. 8, pp. 181590–181604, 2020.

[18] Medetec, “Medetec wound image database,” Medetec Medical Images, [Online]. Available: Medetec Medical Images. Accessed Dec. 2, 2025.

[19] C. Wang, D. M. Anisuzzaman, V. Williamson, M. K. Dhar, B. Rostami, J. Niezgoda, S. Gopalakrishnan, and Z. Yu, “Fully automatic wound segmentation with deep convolutional neural networks,” Scientific Reports, vol. 10, p. 21897, 2020.

[20] S. R. Oota, V. Rowtula, S. Mohammed, M. Liu, and M. Gupta, “WSNet: towards an effective method for wound image segmentation,” in Proc. IEEE/CVF Winter Conf. Applications of Computer Vision (WACV), 2023, pp. 3233–3242.

[21] CVAT.ai Corporation, “CVAT: computer vision annotation tool, v2.16.1,” Zenodo, 2024.

[22] O. Oktay, J. Schlemper, L. Le Folgoc, M. C. H. Lee, M. Heinrich, K. Misawa, K. Mori, S. G. McDonagh, N. Y. Hammerla, B. Kainz, B. Glocker, and D. Rueckert, “Attention U-Net: learning where to look for the pancreas,” unpublished.

[23] M. Alabdulhafith, A. S. Ba Mahel, N. A. Samee, N. F. Mahmoud, R. Talaat, M. S. A. Muthanna, and T. M. Nassef, “Automated wound care by employing a reliable U-Net architecture combined with ResNet feature encoders for monitoring chronic wounds,” Frontiers in Medicine, vol. 11, p. 1310137, 2024.

[24] J. Shen, J. Qin, G. Chen, Y. Cui, G. Li, and Y. Miu, “DCSCSA U-Net: a deeper and compact spatial-channel synergistic attention U-Net for scar segmentation and detection,” IEEE Access, vol. 13, pp. 149765–149776, 2025.

[25] L. R. Dice, “Measures of the amount of ecologic association between species,” Ecology, vol. 26, no. 3, pp. 297–302, 1945.

[26] K. Pearson, “Mathematical contributions to the theory of evolution. On a form of spurious correlation which may arise when indices are used in the measurement of organs,” Proc. Roy. Soc. London, vol. 60, pp. 489–498, 1897.

[27] O. Ronneberger, P. Fischer, and T. Brox, “U-Net: convolutional networks for biomedical image segmentation,” unpublished.

[28] M. Z. Alom, M. Hasan, C. Yakopcic, T. M. Taha, and V. K. Asari, “Recurrent residual convolutional neural network based on U-Net (R2U-Net) for medical image segmentation,” unpublished.